Shading correction algorithm for improvement of cone beam CT images in radiotherapy.

T E Marchant, C J Moore, C G Rowbottom, R I Mackay and P C Williams

North Western Medical Physics, Christie Hospital NHS Foundation Trust, Manchester, M20 4BX, UK.

Abstract. Cone beam CT (CBCT) images have recently become an established modality for treatment verification in radiotherapy. However, identification of soft tissue structures and the calculation of dose distributions based on CBCT images is often obstructed by image artefacts and poor consistency of density calibration. A robust method for voxel by voxel enhancement of CBCT images using a priori knowledge from the planning CT scan has been developed and implemented. CBCT scans were enhanced using a low spatial frequency grey scale shading function generated with the aid of a planning CT scan from the same patient. This circumvents the need for exact correspondence between CBCT and CT and the process is robust to the appearance of un-shared features such as gas pockets. Enhancement was validated using patient CBCT images. CT numbers in regions of fat and muscle tissue in the processed CBCT were both within 1% of the values in the planning CT, as opposed to 10-20% different for the original CBCT. Visual assessment of processed CBCT images showed improvement in soft tissue visibility, although some cases of artefact introduction were observed.

1   Introduction

A recent advance in radiotherapy imaging has been the integration of kilovoltage X-ray sources and amorphous silicon imaging panels onto commercially available medical linear accelerator gantries. This allows digital, rotational fluoroscopy to be performed in support of cone-beam CT (CBCT) reconstructive imaging (Jaffray *et al.*, 2002; Letourneau *et al.*, 2005). Since CBCT images are three dimensional (3D) they can be compared to treatment planning images to determine patient set-up errors from the displacement of bony anatomy in all directions (Guckenberger *et al.*, 2006; Borst *et al.*, 2007). Alternatively they can be used to assess the position of a target structure using soft tissue detail that is much improved compared to the mega-voltage X-ray (MV) portal imaging modalities (Smitsmans *et al.*, 2005). While CBCT offers greater soft tissue detail than MV portal imaging, the presence of image artefacts causes difficulties in identification of soft tissue structures. Significant artefacts are due to X-ray scatter, motion and detector panel persistence.

Once deviations from the planned patient position have been observed using CBCT imaging it is important to be able to assess what consequence this has for the treatment in terms of the dose received by the target and organs at risk. Ideally the daily delivered dose distribution would be calculated based on the patient representation observed in the CBCT. In order to do this it must be possible to calibrate the CBCT voxel values in terms of electron density, used by the treatment planning system in the calculation of dose deposition. This relationship is straightforward to measure for fan beam CT systems using a contrast phantom with inserts of known density (Thomas, 1999). The calibration is more difficult for CBCT systems due to the much larger influence of X-ray scatter when using a wide, cone-beam of X-rays (Siewerdsen and Jaffray, 2001). Scatter in CBCT gives rise to artefacts which are dependent of the size and shape of the object being imaged, and cause variations in reconstructed density with spatial location in the object. This degrades the global relationship between reconstructed voxel value and electron density, making identification of soft tissue structures more difficult and introducing errors into dose calculations based on CBCT images.

The need to minimize scatter artefacts in wide-angle CBCT has been recognized by a number of authors. Physical modifications to the image acquisition equipment such as anti-scatter grids (Siewerdsen *et al.*, 2004) and beam filters (Graham *et al.*, 2007; Moore *et al.*, 2006b) have been investigated, showing some reduction in scatter artefacts. Software corrections to CBCT images both pre (Siewerdsen *et al.*, 2006; Rinkel *et al.*, 2007) and post (Moore *et al.*, 2006a; Morin *et al.*, 2007) reconstruction have also been described. However, these methods of scatter reduction are not available on all commercial systems, and, while significant improvements may result, the elimination of scatter artefacts for all sizes of object has not yet been achieved. Other artefacts are present in CBCT images, which compound the problems of X-ray scatter, including motion artefacts (Yang *et al.*, 2007) and effects due to detector panel persistence (Siewerdsen and Jaffray, 1999).

A number of authors have considered the problem of how to derive density information for radiotherapy dose calculations from CBCT images in the presence of artefacts. These can be split into methods which assign a uniform density value to different regions of the image, and those applying correction factors to the CBCT image itself. In the former group, Boggula *et al.* (Boggula *et al.*, 2007) replaced CBCT pixel values identified as air, soft-tissue or bone with the mean value from the corresponding regions in the reference CT image. In (van Zijtveld *et al.*, 2007) van Zijtveld *et al.* used mapping of reference CT values onto CBCT images after bony registration and respecting CBCT patient/air boundaries. Chi *et al.* (Chi *et al.*, 2007) used a modified or 'stepwise' density table to assign single density values to CBCT pixels values within

specified ranges. These methods are used to generate density information for dose calculation purposes only, and produce little or no enhancement of CBCT image itself.

The application of correction factors to the CBCT image for correction of density values has the additional potential advantage of enhancing image quality for tissue visualization. Examples of this approach include the generation of a look-up table to convert CBCT pixel values into HU by matching landmarks in CT and CBCT image histograms (Depuydt *et al.*, 2006), an ellipsoidal cupping correction applied to mega-voltage CBCT images (Morin *et al.*, 2007), and a polynomial correction map generated from pixel values identified as muscle tissue in CBCT images (Zijp *et al.*, 2007).

In this paper we describe a post-processing method of correcting artefactual density variations in CBCT images based on a comparison to the planning (fan beam) CT images, which are commonly available for radiotherapy patients. We also describe the results of applying this correction method for a group of prostate cancer patients. This is a pragmatic approach to allow improvement of imperfect images from current commercially available CBCT scanners. Pre-processing techniques, which identify and eliminate artefacts from the projection data, would be advantageous where available. However, post-processing techniques also have some attractive features, since they do not require access to the raw projection data, so can be applied retrospectively by the end-user and are not specific to a particular scanner manufacturer.

2   Materials and Methods

2.1   Image data
CBCT images were acquired with the Elekta Synergy imaging system (XVI 3.5, Elekta, Crawley, UK). Phantom and prostate patient images were acquired at 120kV with approximately 650 x-ray projection images giving a weighted dose (1/3 central plus 2/3 peripheral dose) of 9mGy. Images were reconstructed with 1 mm cubic voxels covering a field of view of 41x41x12 cm in the lateral, vertical and longitudinal directions respectively. The CBCT images were then averaged in the longitudinal direction to produce 3 mm slice width. CBCT image correction algorithms were tested using Rando (The Phantom Laboratory) anthropomorphic phantom images and six prostate IMRT patients with 5 CBCT images each. Reference CT images were acquired with a GE Highspeed CT/i scanner (GE Medical Systems) at 120kV with 5 mm slice width, and pixel size 0.8-1.0 mm within each slice.

2.2   CBCT correction method
The method for correcting CBCT pixel values consists of two steps. The first is a global linear scaling to account for differences in normalization between the CT and CBCT images. This is necessary as the CBCT system used is optimized as a set-up and soft tissue visualization tool, which is not currently intended to produce pixel values calibrated as Hounsfield Units. The second step corrects variations in density in different regions of the image caused by a range of phenomena e.g. scatter, detector persistence and motion. The pattern of these artefacts is dependent on the object being imaged, so the correction takes the form of a customized filter derived by comparison of each CBCT image with the corresponding reference CT. Processing of the CBCT images was implemented using IDL (v6.3, ITT Visual Information Systems).

2.2.1   Global normalisation correction
Initially the range of pixel values in the CT and CBCT images is different, see Figure 1a showing the histogram for each. Two main peaks are present in both histograms corresponding to air and soft-tissue regions in the images. The peaks in the reference CT histogram are narrower with the soft tissue peak well differentiated into two sub-peaks corresponding to fat and muscle tissue. The

peaks in the CBCT image are wider and the soft tissue peak shows less differentiation of different tissue types. This is due to increased noise in the CBCT image and artefacts that cause the same tissue type in different regions of the image to have variable density. Initially the peak positions in the CBCT image histogram do not coincide with the peaks in the CT image histogram. The whole CBCT image, *CBCT*, is linearly scaled to give a normalized CBCT image, *nCBCT*, where

$$nCBCT = CBCT*a + b \qquad (1)$$

with *a* and *b* selected to give the closest fit (sum of squared difference) between the two histograms. Figure1b shows the CBCT image histogram after the scaling has been applied.
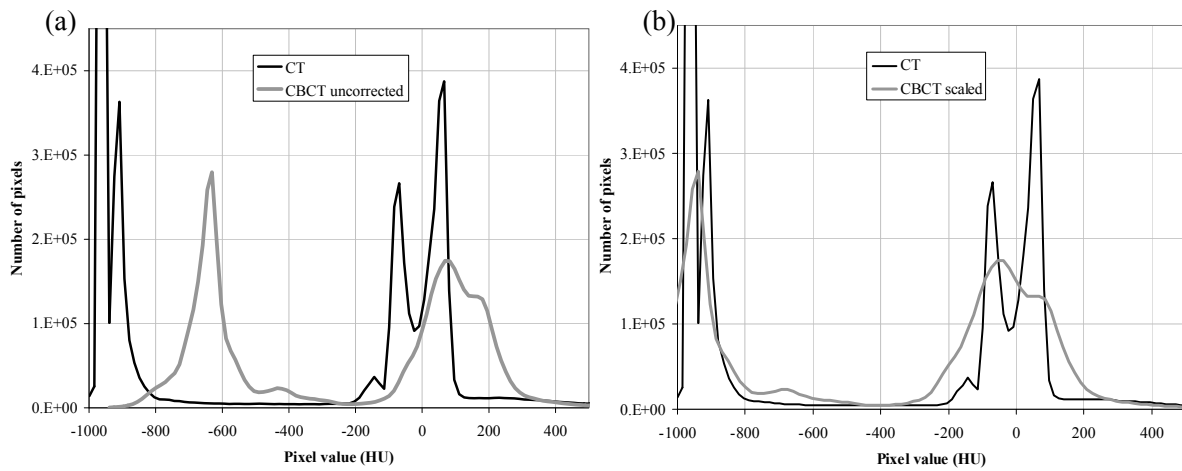
Figure 1. Global image histograms of CT and CBCT images. (a) Before linear scaling of CBCT image and (b) after linear scaling of CBCT image.

2.2.2 *Shading correction*

The images obtained from the CBCT scan suffer from artefacts in the form of spurious brightness variations in different regions of the image. These variations are generally slowly varying and can be identified by comparison with the pre-treatment CT scan. The pre-treatment CT scan is used as a reference for the correct brightness in each region of the image. The two images are aligned and one image is divided by the other to produce a ratio image that indicates the difference between the two images. This image cannot be used directly to correct the CBCT image, as this would simply transform the CBCT into the CT image. Only slowly varying differences in density are to be corrected. Hence the ratio image is smoothed to prevent any high spatial frequency content (edges) from being transferred between the two images. The smoothing is done using a boxcar averaging over a width of 15mm. The smoothed ratio image (referred to as a "shading map") is subsequently used to correct the CBCT by division.

A further concern is that certain regions of the two images are not directly comparable. For example, due to changes in the patient's shape there may be some regions that are inside the patient in one image but not in the other. Similarly, there may be gas in the rectum in one image but not in the other. Patient deformation and slight mis-alignments of the images may also lead to regions of bone being non-comparable between the images. To avoid these problems regions of air and bone in each image are identified using a simple threshold (see details in Appendix). These non-comparable regions are considered as missing data and linear interpolation from surrounding regions is used to fill them in. Interface regions are also excluded by expanding the areas identified as bone/gas by a small amount before the interpolation.

Bone density in the CBCT images was found to be lower than the reference CT images. Hence a different shading map was used within regions identified as bone on the CBCT. In these regions a shading map that does not treat bone as missing data was used.

Appendix I contains a detailed description of all steps of the correction algorithm in equation form. The flowchart in Figure 2 outlines the shading correction process and the sequence of images in Figure 3 shows the reference CT, normalised CBCT, derived shading map and shading corrected CBCT. The CT and CBCT images in Figure 3a, b and d are displayed with the same window setting of -200 to +200 HU. Application of the shading correction to a CBCT image with 40 slices of equivalent slice width 3 mm takes approximately 2 minutes to complete on a Sun Fire V250 workstation with 1.28 GHz CPU.

```
┌──────────────┐        ┌──────────────┐
│  CT image    │        │  CBCT image  │
└──────┬───────┘        └──────┬───────┘
       │                       │
       ▼                       ▼
┌──────────────────────────────────────────┐
│ Linear scaling of CBCT image using image  │
│               histograms                  │
└──────────────────┬───────────────────────┘
                   ▼
┌──────────────────────────────────────────┐
│      Image registration: CT to CBCT       │
└──────┬─────────────────────────┬──────────┘
       ▼                         ▼
┌─────────────────────┐  ┌─────────────────────┐
│ Remove regions of   │  │ Remove regions of   │
│ bone and gas        │  │ gas and fill by     │
│ and fill by         │  │ interpolation       │
│ interpolation       │  │                     │
└─────────┬───────────┘  └─────────┬───────────┘
          ▼                        ▼
┌─────────────────────┐  ┌─────────────────────┐
│ Create shading map A:│  │ Create shading map B:│
│ Divide CBCT by CT    │  │ Divide CBCT by CT    │
│ and smooth           │  │ and smooth           │
└─────────┬───────────┘  └─────────┬───────────┘
          ▼                        ▼
┌─────────────────────┐  ┌─────────────────────┐
│ Create enhanced CBCT │  │ Create enhanced CBCT │
│ image A: divide CBCT │  │ image B: divide CBCT │
│ by shading map       │  │ by shading map       │
└─────────┬───────────┘  └─────────┬───────────┘
          ▼                        ▼
┌──────────────────────────────────────────┐
│ Combine enhanced CBCT images: Image B     │
│ within bone regions, Image A elsewhere    │
└──────────────────┬───────────────────────┘
                   ▼
           ┌──────────────┐
           │ Enhanced CBCT │
           └──────────────┘
```

Figure 2. Flowchart of CBCT shading correction process.
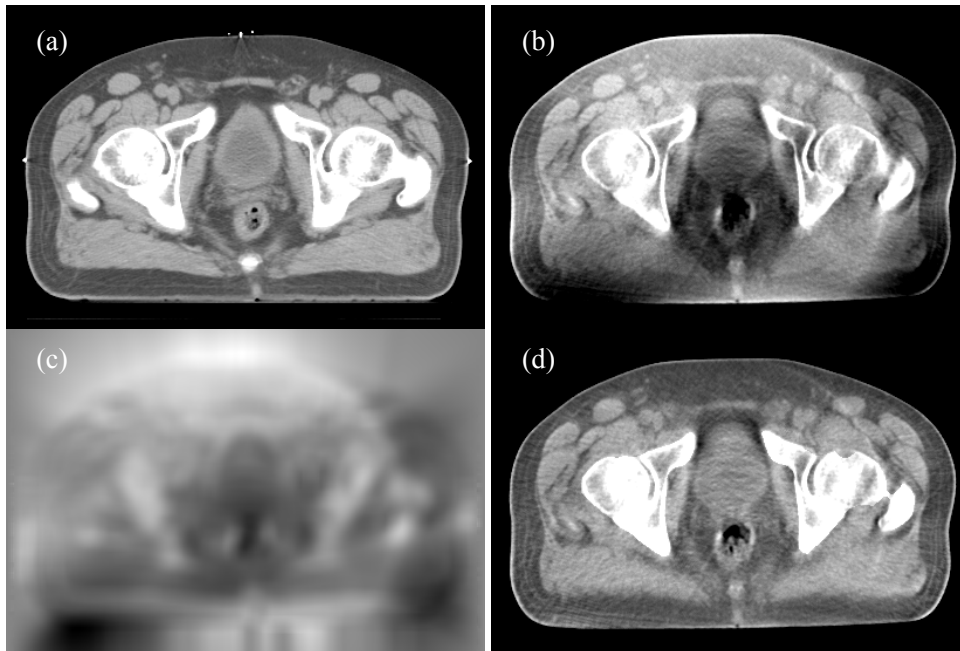
Figure 3. (a) reference CT image (b) normalised CBCT image (c) shading map (d) shading corrected CBCT image.

2.2.3   Comparison of anthropomorphic phantom images

A CBCT image of the Rando phantom pelvis was corrected using the method described above. The image was registered to the planning CT image and pixel by pixel differences between the images were analysed by subtracting the CT from both the raw and corrected CBCT. Image histograms of the subtracted images were computed to show remaining differences.

2.2.4   Comparison of patient outlines

The position of the patient surface is of great importance in determining the dose delivered at a point within the patient. It is therefore essential to check that the position of the patient surface is not changed by the grey level correction procedure described above. The patient surface was outlined for corrected and uncorrected CBCT images. Outlining was done automatically using a threshold level 60% of the value at the skin surface (corrected for the air value not being zero in the uncorrected CBCT). The maximum difference between the two sets of outlines was measured. In addition the patient surface position was also checked using source to surface distances (SSDs) computed by the Pinnacle treatment planning system (Philips Radiation Oncology Systems) for each beam of the treatment plans for six prostate patients with five CBCT images each both before and after correction.

2.2.5   Comparison of patient images

Prostate patient CBCT images before and after calibration were compared to the corresponding reference CT image. Regions of similar tissue type were outlined on each image and the pixel values compared in terms of the mean and standard deviation. The images were also compared visually to assess the performance of the shading correction algorithm, particularly in regions of significant change between reference CT and CBCT.

3   Results

3.1   CBCT correction method

3.1.1   Comparison of anthropomorphic phantom images

Figure 4a shows the histogram of the anthropomorphic phantom CT image subtracted from the corrected and uncorrected CBCT images. The histogram of the corrected CBCT image has a mean value much closer to zero and a much smaller standard deviation. Figure 4b shows the image histograms of the CT, uncorrected CBCT and corrected CBCT. The main peak for the corrected CBCT is much closer to the reference CT and is not as wide as the uncorrected CBCT. The peak for the corrected CBCT is still wider than the CT. This is due to residual artefact in the corrected CBCT and a greater degree of noise than the CT.
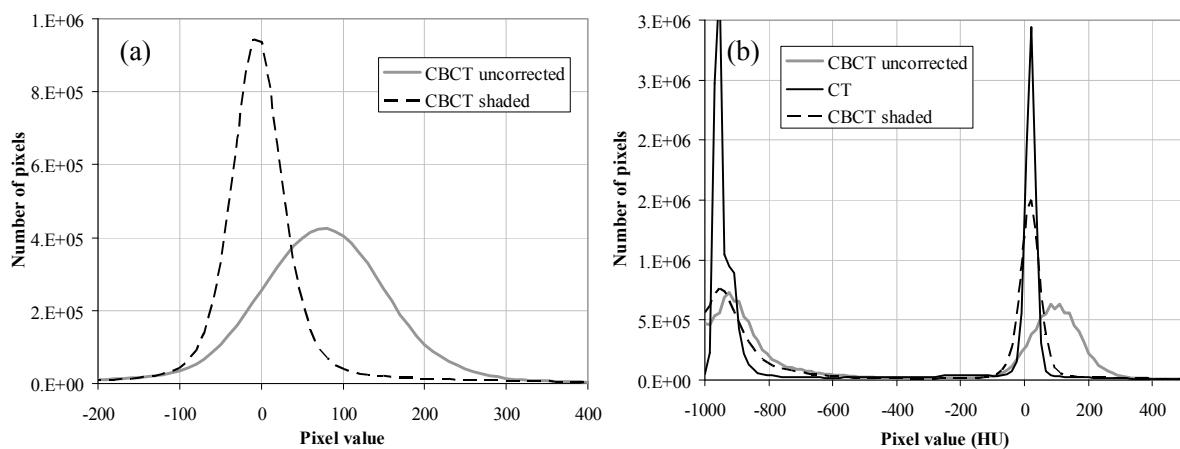
Figure 4. (a) Histograms of subtracted Rando phantom images, dashed line shows difference between the shading corrected CBCT and the CT, solid grey line shows difference between the uncorrected CBCT and the CT, (b) histograms of the uncorrected CBCT (solid grey line), shading corrected CBCT (dashed line) and CT (solid black line)

3.1.2   Comparison of patient outlines

Examination of patient surface contours in CBCT images before and after the shading correction revealed no significant differences, with a maximum observed difference of 1mm. Differences in SSDs before and after the shading correction were always less than 1.5mm and less than 1mm in 95% of cases.

3.1.3   Comparison of patient images

Figures 3b and 3d show a CBCT image before and after the shading correction is applied, displayed using the same window width and window level setting. It is observed that the density in the corrected image is more uniform, particularly the posterior oblique regions of reduced density in the uncorrected CBCT and the anterior region of increased density. The bright ring artefact on the right side of the image is caused by persistence effects in the imaging panel. The severity of this artefact has been greatly reduced, although a residual ring is still visible in the corrected CBCT. This is because only low spatial frequency components of the artefact are removed by the shading correction.

Figure 5 shows image histograms for a patient CBCT image after application of the shading correction and for the corresponding planning CT. This can be compared to the uncorrected

CBCT image histogram shown in figure 1a. After shading correction the CBCT histogram is much closer to the planning CT histogram, with better differentiation between fat and muscle.
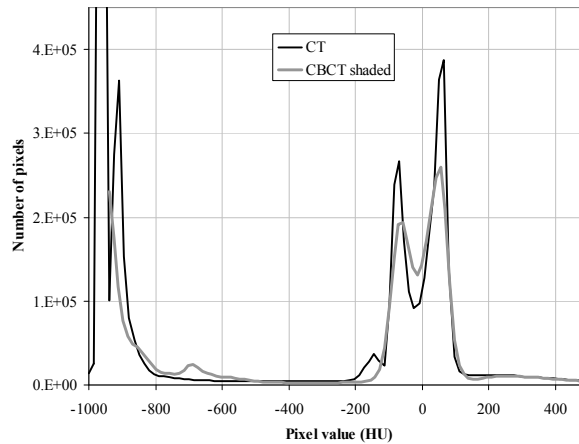
Figure 5. Image histograms for planning CT image (solid black line) and shading corrected CBCT (grey line).

Areas of similar tissue type were outlined on the CBCT and the planning CT. The mean and standard deviation of the grey values were compared. The regions outlined are shown in Figure 6, and the results are shown in Table 1. The fat and muscle uncorrected CBCT grey values were 18% and 12% higher respectively than similar tissue regions in the planning CT image. Linear scaling of the CBCT image improved the agreement for the soft tissue regions (to 5% and 3% high respectively for fat and muscle), but worsened agreement for the bone region. The shading corrected CBCT image showed agreement within 1% for both of the soft tissue regions, and improved agreement for the bone region. Further measurements of fat and muscle regions in different locations were made for CBCT images of six different patients. Shading corrected CBCT regions all agreed with the planning CT values within 1%, while linearly scaled CBCT showed differences of up to 14%. This reflects the intensity variations in different areas of the CBCT image, which are not removed by the linear scaling correction.
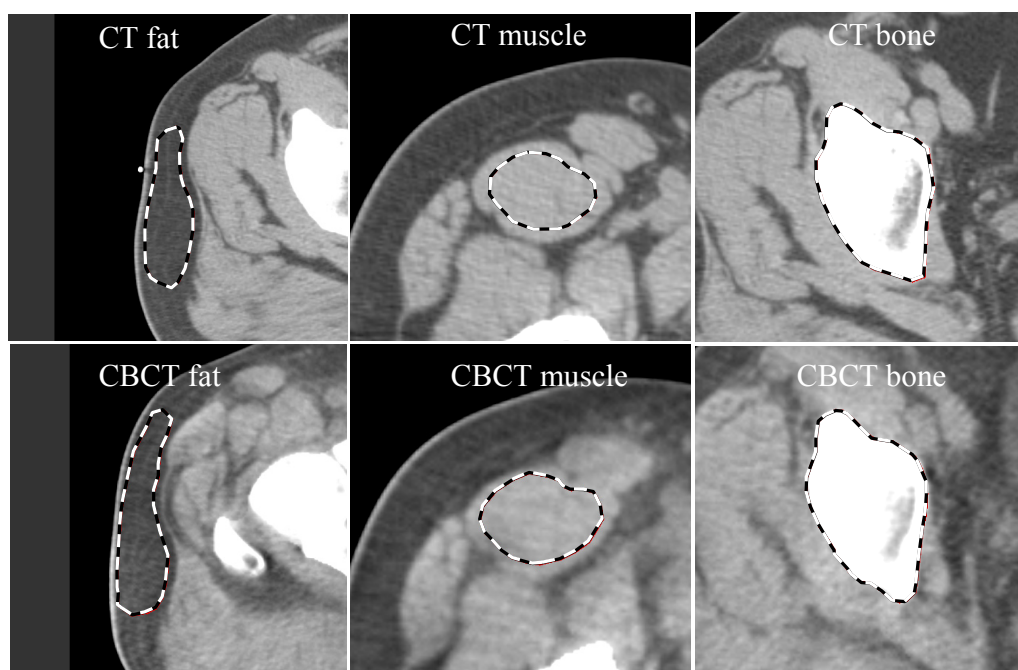
Figure 6. Tissue regions outlines for planning CT and shading corrected CBCT.

Table 1. Mean and standard deviation of grey values in known tissue regions for planning CT, uncorrected CBCT, linearly scaled CBCT and shading corrected CBCT.

	Planning CT	CBCT uncorrected	CBCT linear scaling	CBCT shading corrected
Body	33 ± 154	122 ± 98	6 ± 123	23 ± 130
Fat	-77 ± 13	91 ± 21	-33 ± 26	-77 ± 17
Muscle	76 ± 13	205 ± 11	110 ± 14	69 ± 16
Bone	427 ± 235	350 ± 116	292 ± 145	381 ± 166

Figure 7 shows the effect that shading correction has on a soft tissue structure, the rectum, which has clearly changed shape between the planning CT and CBCT images. Figures 7a and b show the rectum as seen in the planning CT and uncorrected CBCT respectively. Figure 7c also shows the uncorrected CBCT, but with a narrower display window setting, as might be used to visualize the soft tissue organs of the pelvis. When using this narrower window setting the rectal border is no longer visible. Figure 7d shows the shading corrected CBCT, again with the narrower window setting. Here the rectal border is clearly visible, allowing the narrower window setting to be used. The shape of the rectum that was present in the original CBCT image (figure 7b) has been preserved, without being influenced by the clearly different rectal shape in the planning CT (figure 7a). Visualization of soft tissue organs adjacent to the rectum is much easier using the shading corrected image than the original CBCT, because a narrower display window setting can be comfortably used.
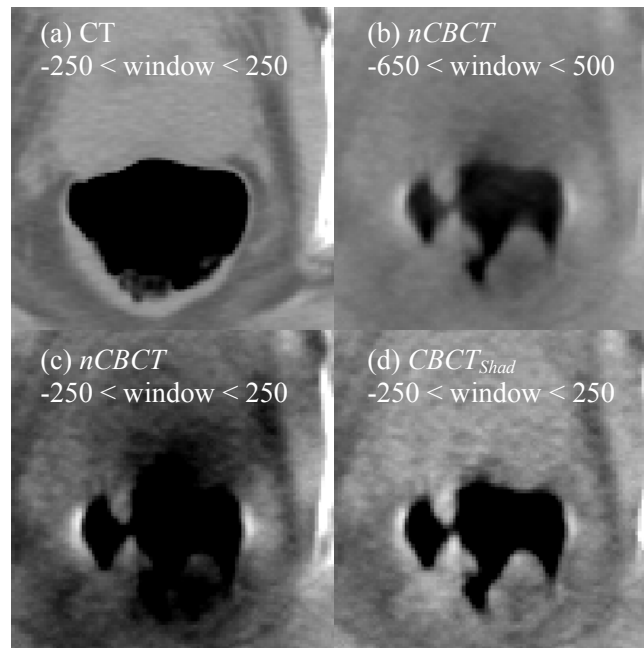
Fig. 7. (a) Planning CT rectum displayed with window lower level (WL) -250 and window upper level (WU) 250, (b) *nCBCT* rectum displayed with WL -650 and WU 500, (c) *nCBCT* rectum displayed with WL -250 and WU 250, (d) Shading corrected CBCT rectum displayed with WL -250 and WU 250.

Figure 8 shows the effect of the shading correction on images of the bladder for a case where the bladder filling was variable between the reference CT and the CBCT images. Figure 8a shows the reference CT bladder, which is smaller than the CBCT bladder, shown in figure 8b. Figure 8c shows the CBCT bladder after application of the shading correction. It can be seen that the image values within the bladder have been altered by the correction algorithm, in particular there is a darkening towards the superior border. However, the edges of the bladder are still clearly visible in the corrected image.
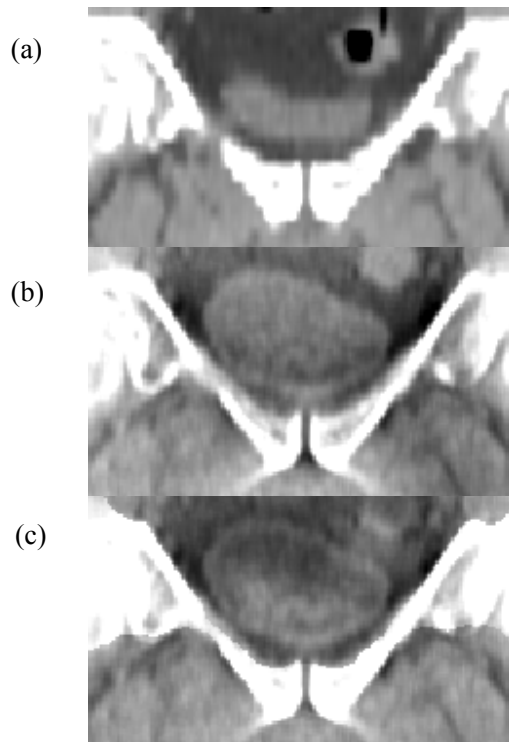
Fig. 8. Effect of shading correction on bladder images. Coronal slices through (a) reference CT (b) original CBCT image (c) shading corrected CBCT image.

4   Discussion

The CBCT shading correction method presented here can be considered as an adaptive high pass filtering, in which the reference CT is used to derive a customized filter. This removes low frequency artefactual variations in brightness but not sharp features. A related technique, homomorphic filtering, has been used to normalize brightness in medical images (Johnston *et al.*, 1996), generally by filtering out low spatial frequencies. However, a general high-pass filter cannot distinguish brightness changes caused by artefacts from those that represent genuine detail in the image. The method described here avoids this problem by specifying the expected low frequency distribution, as in the reference CT image.

The method for CBCT pixel value correction described here has some advantages when compared with others described in the literature. The cupping correction for MV CBCT described by Morin *et al.* (Morin *et al.*, 2007) alters density values according to fixed elliptical function. This does not take account of the dependence of scatter artefacts on the object size and shape, hence it is likely to only work for a limited range of objects. The histogram based method of Depuydt *et al.* (Depuydt *et al.*, 2006) has similarities to the global scaling used as a pre-processing step here (see equation 1), although their approach allows the scaling to be non-linear. However, a globally defined look-up table does not account for artefactual density variations in different regions of the image. The method of Zijp *et al.* (Zijp *et al.*, 2007) of identifying muscle tissue has the advantage of not requiring a reference CT image, but may not perform well close to the skin surface where little muscle tissue is present and some of the largest variations in CBCT pixel values are observed to occur.

A concern with using the shading corrected CBCT for radiotherapy dose calculations is that the low spatial frequency component of the image has been forced to be identical to the planning CT. Since the dose distribution is primarily a low spatial frequency function of the density distribution, it may appear that the dose distribution will be biased towards that calculated from the planning CT image. This possibility is avoided because the position of important boundaries in the CBCT images, such as the external patient contour and internal gas pockets, are preserved by the algorithm. Hence the low spatial frequency component of the corrected image is not the same as the planning CT image in these key regions. This is illustrated by figure 9f, which shows the difference between the smoothed planning CT image and the smoothed shading corrected CBCT image (the smoothing used here is the same as that used in generation of the shading map). It can be seen that the smoothed images are not identical, particularly in the regions close to the patient surface and regions of rectal gas. Note that the images shown in figure 9 are aligned based on bony anatomy, and in practice there will be additional differences between the images due to set-up variations.
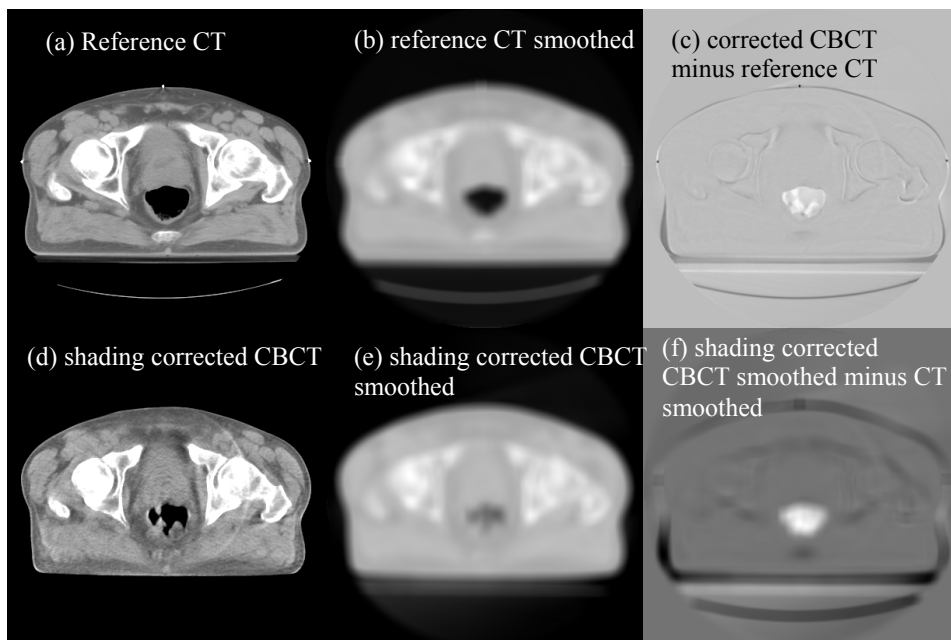
Fig. 9. Effect of shading correction on smoothed image.

The CBCT processing method described here was primarily designed to modify density values in CBCT scans such that accurate radiotherapy dose calculations can be performed. Validation testing of dose calculations using modified CBCT images will be detailed in a separate report. However, it can be appreciated from Figure 3 and Figure 7 that the CBCT images are also enhanced visually by the shading correction. The reduction in shading artefacts allows a narrower window width to be conveniently used when viewing the image, and low contrast details become more visible when no longer masked by the artefactual gradients in the image. Removal of shading artefacts may also improve the performance of deformable registration between CBCT and CT images. The enhancement in image quality is an advantage of our method over other CBCT dose calculation methods based on replacement of CBCT pixel values with bulk values or values transferred from the CT scan (Boggula *et al.*, 2007; van Zijtveld *et al.*, 2007; Chi *et al.*, 2007). There is, however, the possibility that diffuse, low spatial frequency contrast detail may be introduced into the modified CBCT image where a soft tissue structure has changed significantly

between CT planning and CBCT scans, e.g. full and empty bladder as shown in figure 8. Therefore the original CBCT images should be retained for consideration along side the modified CBCT.

5   Conclusion

A post-processing method for enhancement of CBCT images has been developed and validated. The enhancement algorithm increases the accuracy of CBCT density values, allowing soft tissue details to be more easily visualized and enabling use of the CBCT images for dose calculation in radiotherapy.

APPENDIX I. Detailed description of correction algorithm

1. Normalization correction by linear scaling of initial CBCT image, *CBCT*:

$$nCBCT = CBCT*a + b, \tag{A1}$$

where *a* and *b* are chosen to give best match (minimum sum of squared differences) between CBCT and CT image histograms.

2. Image registration of *CT* to *CBCT* and resampling of reference *CT* image onto same voxel locations as *CBCT* to produce CT_{Align}.

3. Create soft tissue masks:

$$CBCT_{mask,\,A} = \begin{cases} 1 \text{ where } T_{CBCT,\,tiss} \leq nCBCT < T_{CBCT,\,bone} \\ 0 \text{ where } nCBCT < T_{CBCT,\,tiss} \text{ OR } nCBCT \geq T_{CBCT,\,bone} \end{cases} \tag{A2}$$

$$CT_{mask,\,A} = \begin{cases} 1 \text{ where } T_{CT,\,tiss} \leq CT_{Align} < T_{CT,\,bone} \\ 0 \text{ where } CT_{Align} < T_{CT,\,tiss} \text{ OR } CT_{Align} \geq T_{CT,\,bone} \end{cases} \tag{A3}$$

The default threshold values used are $T_{CBCT,\,tiss} = 600$, $T_{CBCT,\,bone} = 1300$, $T_{CT,\,tiss} = 850$, and $T_{CT,\,bone} = 1150$.

4. Create soft tissue masks (including bone):

$$CBCT_{mask,\,B} = \begin{cases} 1 \text{ where } nCBCT \geq T_{CBCT,\,tiss} \\ 0 \text{ where } nCBCT < T_{CBCT,\,tiss} \end{cases} \tag{A4}$$

$$CT_{mask,\,B} = \begin{cases} 1 \text{ where } CT_{Align} \geq T_{CT,\,tiss} \\ 0 \text{ where } CT_{Align} < T_{CT,\,tiss} \end{cases} \tag{A5}$$

5. Erode tissue masks:

$$CBCT_{emask,\,A} = \text{erode}(CBCT_{mask,\,A}) \quad \text{(A6)}, \quad CT_{emask,\,A} = \text{erode}(CT_{mask,\,A}) \quad \text{(A7)}$$
$$CBCT_{emask,\,B} = \text{erode}(CBCT_{mask,\,B}) \quad \text{(A8)}, \quad CT_{emask,\,B} = \text{erode}(CT_{mask,\,B}) \quad \text{(A9)}$$

where erode() is an erosion operator with 5mm cube structuring element.

6. Create filled CBCT and CT:

$$CBCT_{fill,\,A} = \begin{cases} nCBCT \text{ where } CBCT_{mask,\,A} = 1 \\[2mm] \text{interpolated value where } CBCT_{mask,\,A} = 0 \end{cases} \quad\quad \text{(A10)}$$

$$CT_{fill,\,A} = \begin{cases} CT_{Align} \text{ where } CT_{mask,\,A} = 1 \\[2mm] \text{interpolated value where } CT_{mask,\,A} = 0 \end{cases} \quad\quad \text{(A11)}$$

$$CBCT_{fill,\,B} = \begin{cases} nCBCT \text{ where } CBCT_{mask,\,B} = 1 \\[2mm] \text{interpolated value where } CBCT_{mask,\,B} = 0 \end{cases} \quad\quad \text{(A12)}$$

$$CT_{fill,\,B} = \begin{cases} CT_{Align} \text{ where } CT_{mask,\,B} = 1 \\[2mm] \text{interpolated value where } CT_{mask,\,B} = 0 \end{cases} \quad\quad \text{(A13)}$$

Linear interpolation in two dimensions is used on a slice-by-slice basis.

7. Create shading maps:

$$Smap_A = \frac{CBCT_{fill,A}}{CT_{fill,A}} \text{ (A14)}, \quad Smap_B = \frac{CBCT_{fill,B}}{CT_{fill,B}} \quad \text{(A15)}$$

8. Smooth shading maps:

$$Smap_{A,sm} = \text{smooth}(Smap_A) \quad \text{(A16)}, \quad Smap_{B,sm} = \text{smooth}(Smap_B) \quad \text{(A17)},$$

where smooth() is a three dimensional boxcar smoothing operator of width 15 mm.

9. Create shading corrected images A and B:

$$CBCT_{Shad,A} = \frac{nCBCT}{Smap_{A,sm}} \text{(A18)}, \quad CBCT_{Shad,B} = \frac{nCBCT}{Smap_{B,sm}} \quad \text{(A19)}$$

10. Create bone mask from shaded CBCT A:

$$BoneMask_{CBCT} = \begin{cases} 1 \text{ where } CBCT_{shad,\,A} \geq T_{CT,\,bone} \\[2mm] 0 \text{ where } CBCT_{shad,\,A} < T_{CT,\,bone,} \end{cases} \quad\quad \text{(A20)}$$

and close bone mask to connect gaps

$$BoneMask_{CBCT} = \text{MorphClose}(BoneMask_{CBCT}), \quad\quad \text{(A21)}$$

where MorphClose() is a morphological closing operator with element size 2.5cm.

11. Combine shaded CBCT images to create final corrected image:

$$CBCT_{shad} = \begin{cases} CBCT_{shad,\,A} \text{ where } BoneMask_{CBCT} = 0 \\ CBCT_{shad,\,B} \text{ where } BoneMask_{CBCT} = 1 \end{cases} \tag{A22}$$

References

Boggula R, Wertz H, Lorenz F, Abo Madyan Y, Boda-Heggemann J, Schneider F, Polednik M, Hesser J, Lohr F and Wenz F 2007 A Proposed Strategy to Implement CBCT Images for Replanning and Dose Calculations (abstract from 49th Annual Meeting of the American Society for Therapeutic Radiology and Oncology) *Int. J. Radiat. Oncol. Biol. Phys.* **69** S655-S6

Borst G R, Sonke J-J, Betgen A, Remeijer P, van Herk M and Lebesque J V 2007 Kilo-Voltage Cone-Beam Computed Tomography Setup Measurements for Lung Cancer Patients; First Clinical Results and Comparison With Electronic Portal-Imaging Device *Int. J. Radiat. Oncol. Biol. Phys.* **68** 555-61

Chi Y, Wu Q and Yan D 2007 Dose Calculation On Cone Beam CT (CBCT) (Abstract from AAPM 49th Annual Meeting, Minneapolis, MN, 22-26 July 2007) *Med. Phys.* **34** 2438-

Depuydt T, Hrbacek J, Slagmolen P and Van den Heuvel F 2006 Cone-beam CT Hounsfield unit correction method and application on images of the pelvic region (Abstract from ESTRO 25, Leipzig, Germany, October 2006) *Radiother. Oncol.* **81** S29

Graham S A, Moseley D J, Siewerdsen J H and Jaffray D A 2007 Compensators for dose and scatter management in cone-beam computed tomography *Med. Phys.* **34** 2691-703

Guckenberger M, Meyer J, Vordermark D, Baier K, Wilbert J and Flentje M 2006 Magnitude and clinical relevance of translational and rotational patient setup errors: A cone-beam CT study *Int. J. Radiat. Oncol. Biol. Phys.* **65** 934

Jaffray D A, Siewerdsen J H, Wong J W and Martinez A A 2002 Flat-panel cone-beam computed tomography for image-guided radiation therapy *Int. J. Radiat. Oncol. Biol. Phys.* **53** 1337-49

Johnston B, Atkins M S, Mackiewich B and Anderson M 1996 Segmentation of multiple sclerosis lesions in intensity corrected multispectral MRI *Medical Imaging, IEEE Transactions on* **15** 154-69

Letourneau D, Wong J W, Oldham M, Gulam M, Watt L, Jaffray D A, Siewerdsen J H and Martinez A A 2005 Cone-beam-CT guided radiation therapy: technical implementation *Radiother. Oncol.* **75** 279-86

Moore C J, Amer A, Marchant T, Sykes J R, Davies J, Stratford J, McCarthy C, MacBain C, Henry A, Price P and Williams P C 2006a Developments in and experience of kilovoltage X-ray cone beam image-guided radiotherapy *The British Journal of Radiology* **79** S66

Moore C J, Marchant T E and Amer A M 2006b Cone beam CT with zonal filters for simultaneous dose reduction, improved target contrast and automated set-up in radiotherapy *Phys. Med. Biol.* **51** 2191

Morin O, Chen J, Aubin M, Gillis A, Aubry J-F, Bose S, Chen H, Descovich M, Xia P and Pouliot J 2007 Dose calculation using megavoltage cone-beam CT *Int. J. Radiat. Oncol. Biol. Phys.* **67** 1201-10

Rinkel J, Gerfault L, Estève F and Dinten J M 2007 A new method for x-ray scatter correction: first assessment on a cone-beam CT experimental setup *Phys. Med. Biol.* **52** 4633-52

Siewerdsen J H, Daly M J, Bakhtiar B, Moseley D J, Richard S, Keller H and Jaffray D A 2006 A simple, direct method for x-ray scatter estimation and correction in digital radiography and cone-beam CT *Med. Phys.* **33** 187-97

Siewerdsen J H and Jaffray D A 1999 Cone-beam computed tomography with a flat-panel imager: Effects of image lag *Med. Phys.* **26** 2635

Siewerdsen J H and Jaffray D A 2001 Cone-beam computed tomography with a flat-panel imager: magnitude and effects of x-ray scatter *Med. Phys.* **28** 220-31

Siewerdsen J H, Moseley D J, Bakhtiar B, Richard S and Jaffray D A 2004 The influence of antiscatter grids on soft-tissue detectability in cone-beam computed tomography with flat-panel detectors *Med. Phys.* **31** 3506-20.

Smitsmans M H, de Bois J, Sonke J J, Betgen A, Zijp L J, Jaffray D A, Lebesque J V and van Herk M 2005 Automatic prostate localization on cone-beam CT scans for high precision image-guided radiotherapy *Int. J. Radiat. Oncol. Biol. Phys.* **63** 975-84

Thomas S J 1999 Relative electron density calibration of CT scanners for radiotherapy treatment planning *The British Journal of Radiology* **72** 781-6

van Zijtveld M, Dirkx M and Heijmen B 2007 Correction of conebeam CT values using a planning CT for derivation of the "dose of the day" *Radiother. Oncol.* **85** 195-200

Yang Y, Schreibmann E, Li T, Wang C and Xing L 2007 Evaluation of on-board kV cone beam CT (CBCT)-based dose calculation *Phys. Med. Biol.* **52** 685-705

Zijp L, Van Herk M, Remeijer P and Sonke J J 2007 Retrospective correction of cupping and shading artifacts in cone beam CT for image guidance without using the planning scan (Abstract from 9th Biennial ESTRO Meeting on Physics and Radiation Technology for Clinical Radiotherapy, Barcelona (Spain), 8-13 September 2007) *Radiother. Oncol.* **84** S177